ELSEVIER

Contents lists available at ScienceDirect

Optics Communications

journal homepage: www.elsevier.com/locate/optcom



Mid-infrared chiral metasurface absorbers with split-ellipse structures

Xiangkai Zeng^a, Daniel Rosenmann^b, David A. Czaplewski^b, Jie Gao^{a,c,*}, Xiaodong Yang^{a,*}



- ^a Department of Mechanical and Aerospace Engineering, Missouri University of Science and Technology, Rolla, MO 65409, USA
- ^b Center for Nanoscale Materials, Argonne National Laboratory, Argonne, IL 60439, USA
- ^c Department of Mechanical Engineering, Stony Brook University, Stony Brook, NY 11794, USA

ARTICLE INFO

Keywords: Chiral metasurface Chiroptical effect Circular dichroism Thermal analysis

ABSTRACT

Natural chiral materials usually have very weak circular dichroism (CD) responses. Here, we design and demonstrate one type of mid-infrared chiral metasurface absorber with strong chiroptical effects, which can achieve high CD in absorption above 0.57 over the wavelength range of 5 to 5.9 μ m. The maximum absorption of the chiral metasurface absorber under circularly polarized light can reach 0.90 and the maximum CD in absorption is 0.63. Meanwhile, the chiral resonance wavelength and the CD value can be tuned by varying the geometric parameters of the metasurface. A thermal analysis of the metasurface absorber further shows the strong connection between CD in absorption and temperature difference. The demonstrated chiral metasurface absorbers can be used in many promising applications such as molecular sensing, thermophotovoltaics and chiral spectroscopy.

1. Introduction

Chirality describes the property of a lack of mirror symmetry in an object, which can be observed in various natural materials [1,2]. However, the circular dichroism of these natural substances under left-handed and right-handed circularly polarized (LCP and RCP) light is extremely small due to the weak chiral light-matter interaction [3]. There are various chiral metamaterial and metasurface structures that are able to exhibit strong chiroptical responses including some that have been recently designed such as letter-shaped structures [4–6], gammadions [7], folded structures [8], slanted holes [9], and stepped nanoapertures [10,11].

These chiral metamaterials and metasurfaces can be utilized in many promising applications in various fields such as biosensing [12–16]. By detecting the wavelength shifts of CD spectra for the biomolecule-deposited chiral metamaterials, the molecular concentration can be quantitively measured with high sensitivity [16], where the wavelength shift is caused by the refractive index variations of the surrounding environment by adding chiral biomolecules. Besides, through the coupling between the chiral electromagnetic field of metamaterials and chiral molecules, the signal-to-noise ratio of CD spectroscopy is increased for realizing highly sensitive biosensing [14,15]. The superchiral fields generated near the chiral nanostructures with the enhanced local optical chirality density will lead to the ultrasensitive detection of chiral molecules in the near-field [17]. The chiral metamaterials and metasurfaces applied to molecular sensing can also be designed in the mid-infrared range to detect the characteristic vibrational fingerprints

of the functional groups in molecules. It has been known that in the mid-infrared frequency range below ~100 THz, the resonance frequency of a plasmonic nanostructure has a linear scaling with the structural size. However, as the resonance frequency is pushed higher to visible and ultraviolet range by reducing the structural size of the plasmonic nanostructure, a breakdown of such linear scaling occurs where the resonance frequency saturates and the strength of the resonance decreases due to the free electron kinetic energy [18]. As a result, it becomes difficult to sustain strong resonant modes in the plasmonic nanostructure for chiral molecular sensing. Alternatively, dielectric nanostructures can be designed for chiral sensing in visible and ultraviolet frequencies, where chiral molecules exhibit the featured electronic fingerprints. In addition, the chiral metamaterials and metasurfaces operating in the mid-infrared wavelength range can be used as the polarization-dependent thermal absorbers and emitters to control the response of a thermophotovoltaics device and increase the thermal energy conversion efficiency. Therefore, it is important to develop chiral metamaterials and metasurfaces with high CD responses in the mid-infrared wavelength range.

In this work, we design and demonstrate a new type of mid-infrared chiral metasurface absorbers using a tri-layer metal–dielectric–metal structure. Within the wavelength range between 5 μ m and 5.9 μ m, the chiral metasurface absorbers can achieve strong chiroptical effects with high CD in absorption above 0.57. The chiral metasurface absorbers can reach a maximum absorption of 0.90 under circularly polarized light and a maximum CD in absorption of 0.63. Such strong chiroptical responses are attained by the design of split-ellipse resonators on

^{*} Corresponding author at: Department of Mechanical and Aerospace Engineering, Missouri University of Science and Technology, Rolla, MO 65409, USA. E-mail addresses: jie.gao.5@stonybrook.edu (J. Gao), yangxia@mst.edu (X. Yang).

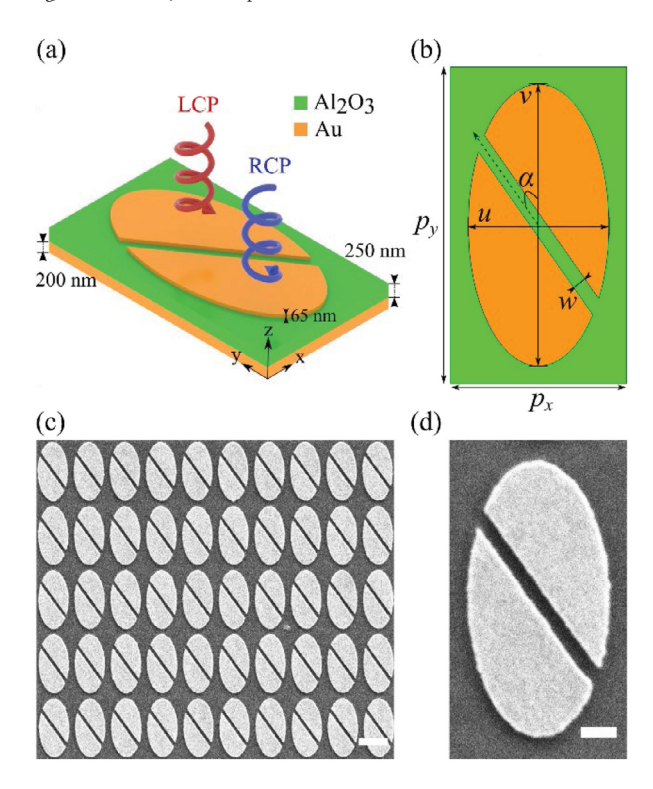


Fig. 1. (a) Schematic of the unit cell of the designed chiral metasurface absorber. (b) Top view of the unit cell and its geometric parameters. (c) SEM image of the fabricated chiral metasurface absorber. Scale bar: 2 µm. (d) SEM image of one unit cell. Scale bar: 500 nm

the top metal layer. Furthermore, it is demonstrated that the chiral resonance wavelength and the CD value can be tuned by varying the geometric parameters of the top-layer metallic pattern. The electric field distributions in the metasurface absorber under LCP and RCP incident light are mapped for understanding the mechanism of chiral optical absorption. The temperature distributions in the metasurface absorber are also simulated to study the relationship between CD in absorption and temperature difference under LCP and RCP incidence. The demonstrated results will have the potential to advance many future applications such as thermophotovoltaics [19–22], chiral imaging [11,23], and chiral molecular sensing [24,25].

2. Design and characterization of mid-infrared chiral metasurface absorbers

The schematic of the designed chiral metasurface absorbers is presented in Fig. 1(a), which is constructed on a tri-layer gold-aluminagold (Au-Al₂O₃-Au) film, including the split-ellipse resonators on the top metal layer of 65 nm-thick Au, the middle dielectric spacer with 250 nm-thick Al₂O₃, and the bottom layer with 200 nm-thick Au deposited on a silicon substrate. The Au layers are deposited with a Lesker PVD250 electron beam evaporator, and the Al2O3 layer is deposited using a Lesker CMS18 reactive sputtering system. The dimension of the split-ellipse resonator is presented in Fig. 1(b). The periods of the unit cell along the x and y directions are $p_x = 2.5 \mu m$ and $p_y = 4.5 \mu m$, respectively. The split-ellipse structure has major and minor axes of $v = 4 \mu m$ and $u = 2 \mu m$, respectively. The width of the cutting slot is w = 200 nm and its rotation angle is $\alpha = 35^{\circ}$. The split-ellipse structure is fabricated by milling the top Au layer with a focused ion beam system (FIB, FEI Helios Nanolab 600, 30 kV, 97 pA). A scanning electron microscopic (SEM) image of the top view of the fabricated chiral metasurface absorber is shown in Fig. 1(c), with a SEM image of the unit cell shown in Fig. 1(d).

The mechanism of chiroptical responses in the designed chiral plasmonic metasurfaces can be understood using the numerical simulations of the plasmonic resonant modes with LCP and RCP illumination by CST Studio Suite. The open boundary conditions are applied along the z direction and the periodic boundary conditions are applied along the x direction and the y direction of the unit cell. The permittivity of Al₂O₃ is extracted from the experimental data [26] and the permittivity of Au is taken from the Lorentz-Drude model [27]. The electric field distributions under LCP and RCP illumination in the plane 5 nm above the lower surface of the top Au layer (z = 455 nm) at the chiral resonance wavelength of 5.04 µm is shown in Fig. 2(a). It indicates that the LCP incident light is strongly coupled to the plasmonic resonant mode of the split-ellipse resonator with matched impedance. The electric field |E| is highly localized in the tip, slot and border areas of the splitellipse structure, which consequently gives strong optical absorption and weak reflection. On the other hand, the electric field |E| excited by the RCP light is much weaker since the incident light cannot efficiently couple with the split-ellipse resonator and most of the input optical power is reflected, yielding weak optical absorption. To further explain the underlying mechanism of the differential absorption in the chiral metasurface absorber, Fig. 2(b) displays the current density distributions under LCP and RCP illumination in the plane of z=455 nm. It shows that under LCP incidence, the generated current density vector J oscillates strongly along the y direction in four confined areas inside the split-ellipse structure, which forms three out-of-phase circulating current loops surrounding the dielectric layer between the top Au layer and the bottom Au layer, so that a strong optical absorption is achieved. On the contrary, J oscillates along the x direction in the split ellipse to form one circulating current loop under RCP incidence with a much weaker |J| value compared to the LCP case, resulting in a weak optical

Furthermore, Fig. 3(a) plots the magnetic field distributions under LCP and RCP illumination in the middle plane of the dielectric layer (z=325 nm). It shows that the LCP incident light excites three strong out-of-phase magnetic dipole modes along the x direction within the dielectric layer, which induce three circulating current loops as indicated in Fig. 2(b). In contrast, the RCP light excites one weak magnetic dipole mode along the y direction with a much weaker intensity. The direction and magnitude of the Poynting vector at z=325 nm is further plotted in Fig. 3(b). Under LCP illumination, the optical energy can be efficiently coupled into the dielectric layer with two strong clockwise energy circulations in the x-y plane, whereas the coupled optical energy for the RCP incident light has a much lower power density value where the two counterclockwise energy circulations in the plane get broken.

To further understand the properties of the chiral plasmonic resonant modes, the distributions of electric field, magnetic field, current density and Poynting vector across the plane of x = 400 nm along the tip of the cutting slot and the plane of x = 1000 nm are also simulated under LCP and RCP illumination in Figs. 4 and 5 respectively, where the two locations are denoted by the white dashed lines in Fig. 2(a). As shown in Fig. 4(a), at x = 400 nm, the concentrated electric field around the metallic split-ellipse structure further extends inside the dielectric layer under LCP illumination, resulting in strong absorption, whereas the electric field in the dielectric layer is much weaker under RCP illumination. Fig. 4(b) shows that a strong magnetic dipole mode along the *x*-direction is excited in the dielectric layer under LCP illumination, which induces a distinct circulating current loop between the top Au layer and the bottom Au layer to give a strong optical absorption. However, there is no circulating current loop observed under RCP illumination. Fig. 4(c) of the Poynting vector further indicates that the optical energy of LCP incident light can flow into the dielectric layer with the enhanced optical absorption, whereas the RCP light energy just flow towards the bottom Au layer and get reflected back. At x = 1000 nm, Fig. 5(a) shows that the electric field around the top Au structure is greatly enhanced under LCP incidence with the electric field vector oscillates along the z-direction, compared to the RCP case.

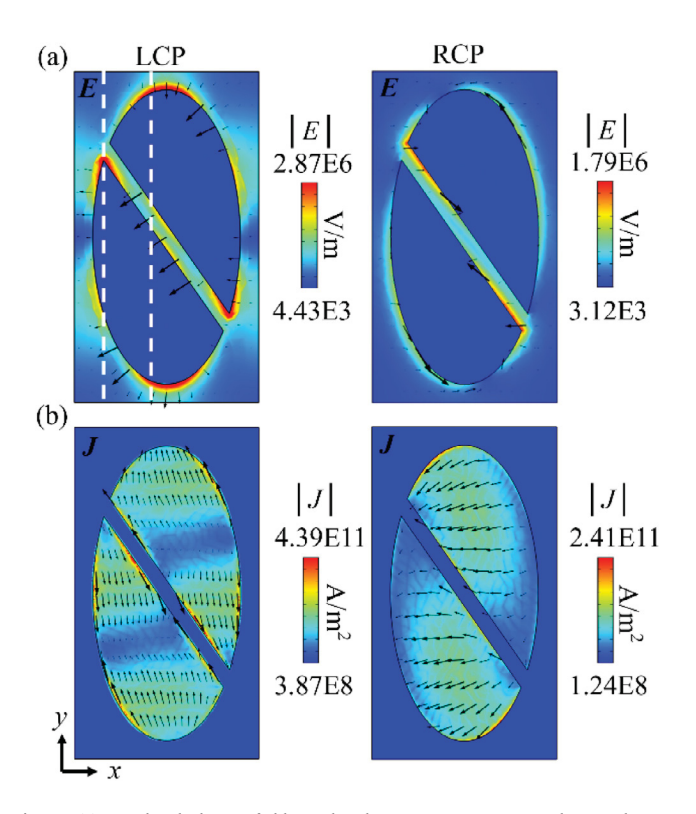


Fig. 2. (a) Simulated electric field |E| distributions at z=455 nm plane under LCP and RCP illumination at the chiral resonance wavelength of 5.04 μm . The black arrows represent the direction and magnitude of the electric field vector E. The two white dashed lines mark the positions of x=400 nm and 1000 nm. (b) Simulated current density |J| distributions at z=455 nm plane. The black arrows represent the direction and magnitude of the current density vector J.

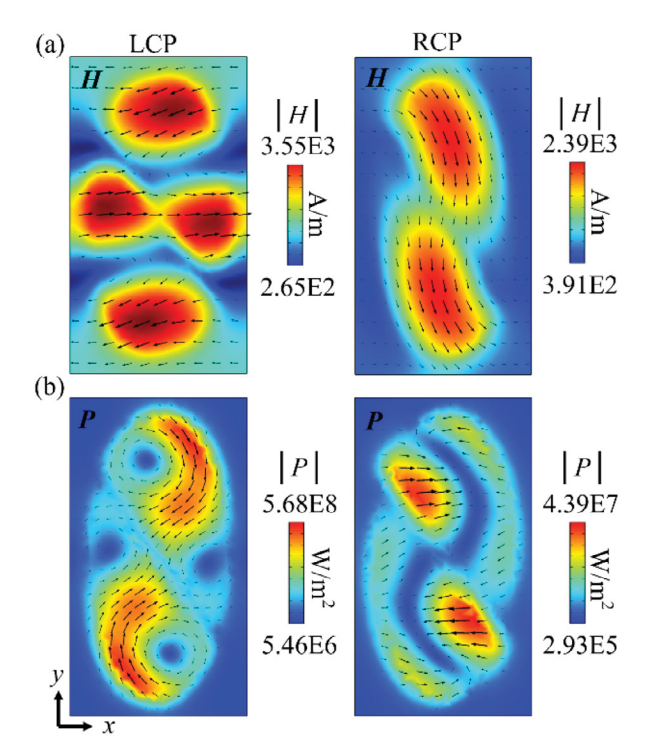


Fig. 3. (a) Simulated magnetic field |H| distributions at z=325 nm plane under LCP and RCP illumination. The black arrows represent the direction and magnitude of the magnetic field vector H. (b) Simulated Poynting vector |P| distributions at z=325 nm plane. The black arrows represent the direction and magnitude of the Poynting vector P

In Fig. 5(b), it is clearly seen that three strong out-of-phase magnetic dipole modes along the x direction are supported within the dielectric layer under LCP illumination, which induce three connected circulating current loops. However, the RCP incident light does not excite such magnetic dipole modes in the dielectric layer. Fig. 5(c) also depicts that the optical energy of LCP light can be efficiently coupled into the dielectric layer with large absorption, but the optical energy of RCP light just gets reflected back from the bottom Au layer without much absorption. Compared to RCP illumination, the strong circular dichroic mode interactions under LCP illumination through the excitation of the magnetic dipole modes and the induced circulating current loops in the split-ellipse structure lead to the large differential absorption in the designed chiral metasurface absorber. Since the 200 nm-thick gold bottom layer can block almost all the transmitted light, the transmission through the metasurface absorber is negligible. Then, the absorption can be defined as A = 1 - R, where A and R represent the absorption and reflection, respectively. The CD in absorption is calculated by CD = $|A_{LCP} - A_{RCP}|$, which is 0.63 from the simulation of this designed chiral metasurface absorber, with a chiral optical absorption of 0.93 under LCP illumination and 0.30 under RCP illumination at the chiral resonance wavelength of 5.04 µm.

To achieve the goal of tuning the chiral resonance wavelength of the metasurface absorber in the mid-infrared wavelength range, the geometric parameters marked in Fig. 1(b) for the split-ellipse structure are linearly scaled up by a factor s, where s = 1, 1.05, 1.1,1.15, and 1.2, while the rotation angle α of the cutting slot remains unchanged. The SEM images of the top view of the fabricated chiral metasurface absorbers in different scales are shown in Fig. 6(a). The optical absorption spectra of these chiral metasurface absorbers are measured by a Fourier transform infrared spectrometer (FTIR, Nicolet 6700) connected to an infrared microscope, with the incident circular polarization defined by a linear polarizer and a quarter-wave plate. The measured and simulated optical absorption spectra are plotted in Fig. 6(b) and (c), respectively. As a result of the scale factor s increasing from 1 to 1.2, the resonance wavelength of the chiral metasurface absorber continuously increases from 5 to 5.9 µm, which is almost proportional to the scale factor. The absorption under LCP illumination is much larger than that under RCP illumination, with the measured CD in absorption more than 0.57 across the wavelength range of 5 to 5.9 µm. The experimental maximum chiral optical absorption is 0.90, while the largest CD in absorption is 0.63 for the metasurface with the scale factor s = 1 at the chiral resonance wavelength of 5.04 μ m.

Furthermore, the chiral resonance wavelength and the CD value can be tuned together by simply adjusting the rotation angle α of the cutting slot. Fig. 7(a) shows the SEM images of the top view of the chiral metasurface absorbers with different rotation angles α . According to the measured and simulated optical absorption spectra in Fig. 7(b) and (c), it is shown that the resonance wavelength decreases from 5.5 to 4.8 μ m when the rotation angle α is increased from 20° to 50°, while the CD value grows from 0.33 to 0.63 as α increases from 20° to 35° and then drops from 0.63 to 0.03 as α keeps increasing to 50°. The small difference between the measured and simulated absorption spectra is possibly introduced by the sample defects during the FIB milling process.

To further understand the effects of different rotation angles and scale factors on the LCP and RCP absorption in the chiral metasurface absorbers, the finite element method solver (COMSOL Multiphysics) is used to solve the heat transfer equation $C_P \rho \partial T/\partial t + \nabla \cdot (-k\nabla T) = q$, where C_P is the specific heat capacity; ρ is the density of the material; T is the temperature; k is the thermal conductivity of the material [6]. The heat generation density q is calculated using the expression of $q(r) = (\omega/2) Im[\varepsilon(\omega)] \varepsilon_0 |E(r)|^2$. For the heat transfer simulation, a 100 nm-thick silicon substrate is considered below the gold bottom layer. Thermal insulation boundary conditions are used around the unit cell in both the x direction and the y direction. A fixed temperature of 300 K is set for the boundary conditions along the z direction at

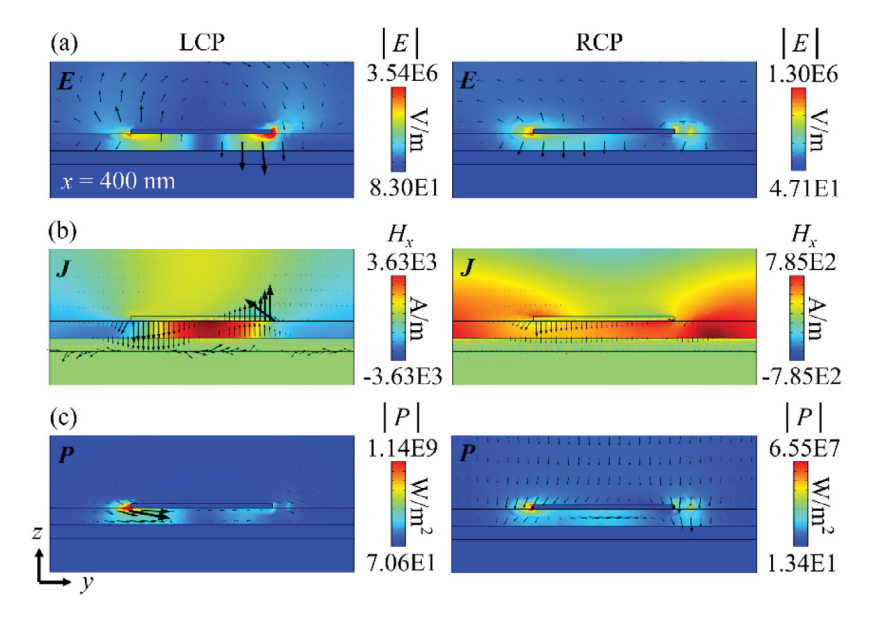


Fig. 4. (a) Simulated distributions of electric field |E| and electric field vector E under LCP and RCP incidence at x = 400 nm plane. (b) Simulated distributions of magnetic field H_x and current density vector J. (c) Simulated Poynting vector distributions of |P| and P.

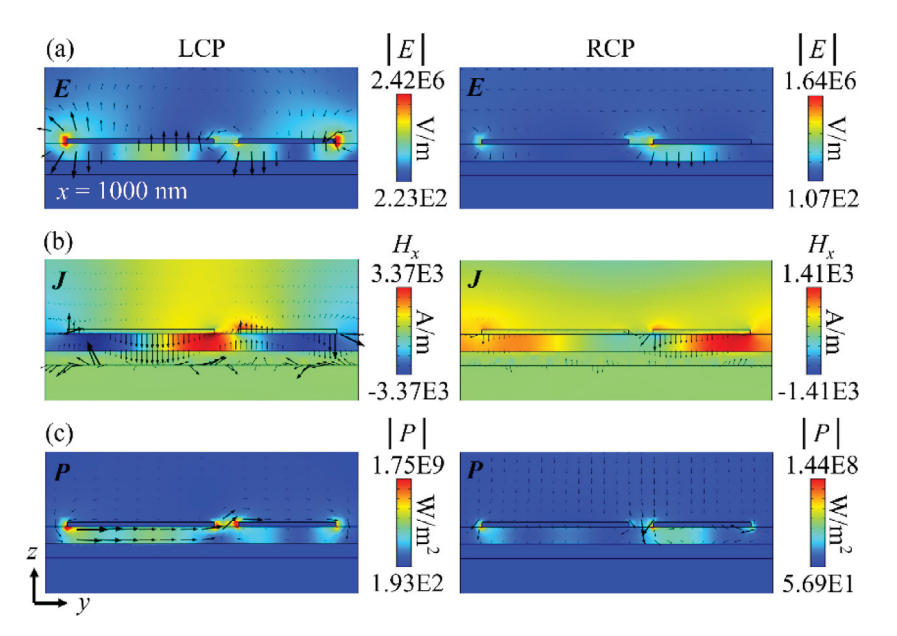


Fig. 5. (a) Simulated distributions of electric field |E| and electric field vector E under LCP and RCP incidence at x = 1000 nm plane. (b) Simulated distributions of magnetic field H_x and current density vector J. (c) Simulated Poynting vector distributions of |P| and P.

the top surface of air and the bottom surface of the silicon substrate. The incident optical power density of the circular polarized light is fixed at 1.78 $\mu W/\mu m^2$. Most of the heat is produced inside the top gold split-ellipse structure, and then the generated heat is diffused into the neighboring media with lower temperature. Fig. 8(a) presents the simulated temperature distributions in the chiral metasurface absorber with the rotation angle α of 35° in the plane at the interface between the upper Au layer and the Al_2O_3 dielectric layer (z=450 nm) under LCP and RCP illumination at the chiral resonance wavelength of 5.04 μm . As presented in Fig. 8(a), the temperature inside the split-ellipse structure is distributed almost uniformly and stays higher than that of its surroundings due to the high thermal conductivity of gold. Fig. 8(b) shows the temperature profiles across the tip of split-ellipse structure which is marked with the white dashed line in

Fig. 8(a). Due to the high absorption of the metasurface under LCP illumination, there is more thermal energy generated so that a large local temperature increase inside the split-ellipse structure is achieved, with a maximum temperature of 333.84 K. On the other hand, the weak chiral optical absorption under RCP illumination gives a much lower maximum temperature of 301.04 K. We can define the thermal circular dichroism (CD_T) as CD_T= $|\Delta T_{LCP} - \Delta T_{RCP}|$ [28], where ΔT represents the temperature increase in the split-ellipse structure under LCP and RCP illumination. The relationship between the values of CD in absorption and CD_T is further studied by simulating the chiral metasurface absorbers with the rotation angle α varying from 20° to 50° for different scale factors s of 1, 1.1 and 1.2. As shown in Fig. 8(c)–(e), the calculated values of CD in absorption and CD_T are strongly correlated for all the chiral metasurface absorbers, with the linear

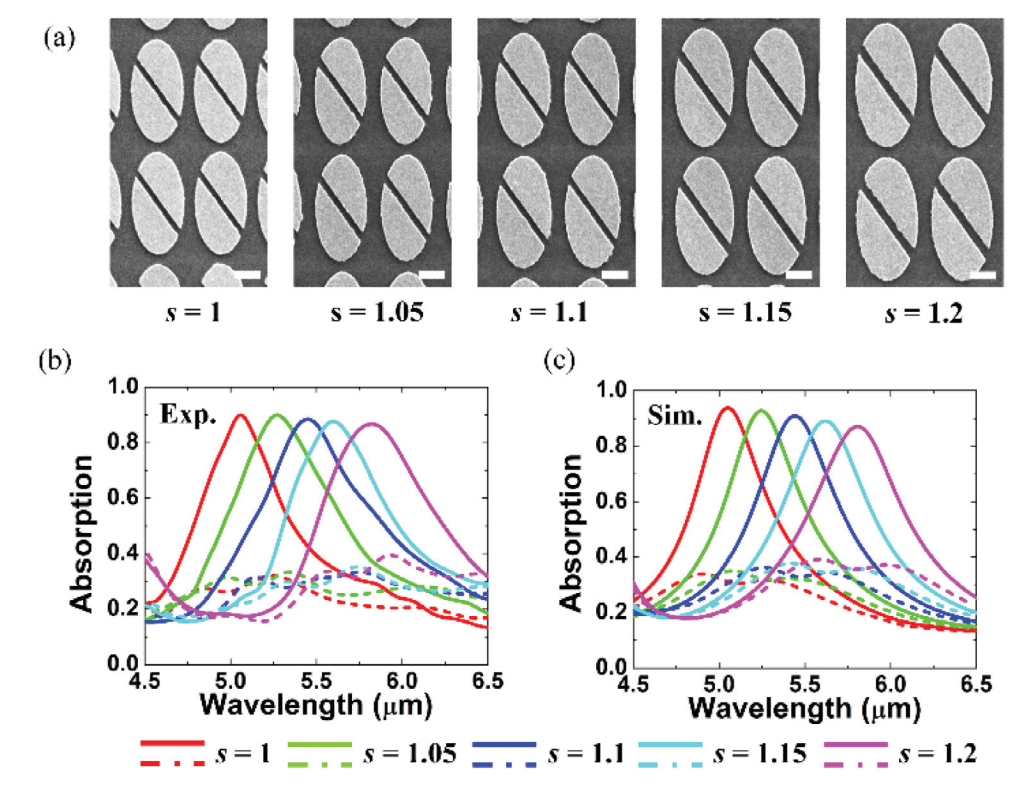


Fig. 6. (a) SEM images of the fabricated chiral metasurface absorbers with different scale factors. Scale bar: 500 nm. (b) Measured and (c) simulated optical absorption spectra of the chiral metasurface absorbers with different scale factors under LCP (solid line) and RCP (dashed line) illumination.

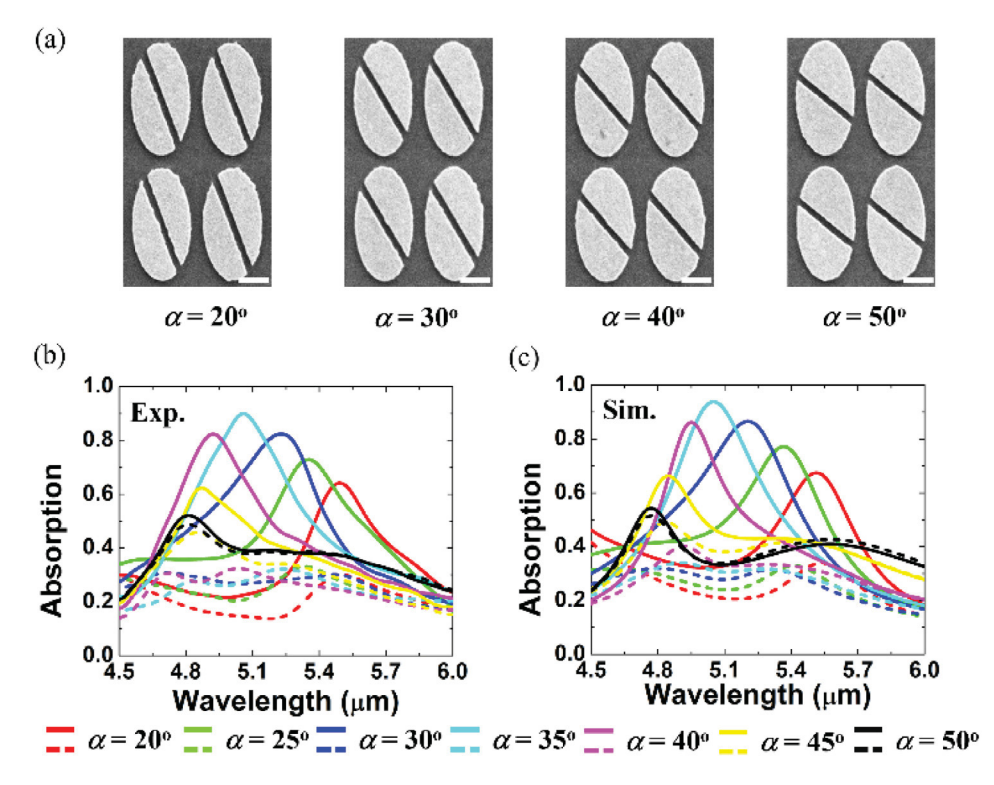


Fig. 7. (a) SEM images of the fabricated chiral metasurface absorbers with different rotation angles. Scale bar: 500 nm. (b) Measured and (c) simulated optical absorption spectra of the chiral metasurface absorbers with different rotation angles under LCP (solid line) and RCP (dashed line) illumination.

relationship of $CD_T=c_T\cdot I_p\cdot CD$, where I_p is the incident optical power density and c_T is a thermal coefficient constant. The data fitting further shows that $c_T=28.26$ K $\mu {\rm m}^2/\mu {\rm W}$ for s=1, $c_T=28.35$

K μ m²/ μ W for s=1.1, and $c_T=28.24$ K μ m²/ μ W for s=1.2, where the minor difference of c_T between different scale factors is due to the imperfections in simulation. It is noted that c_T is a constant with an

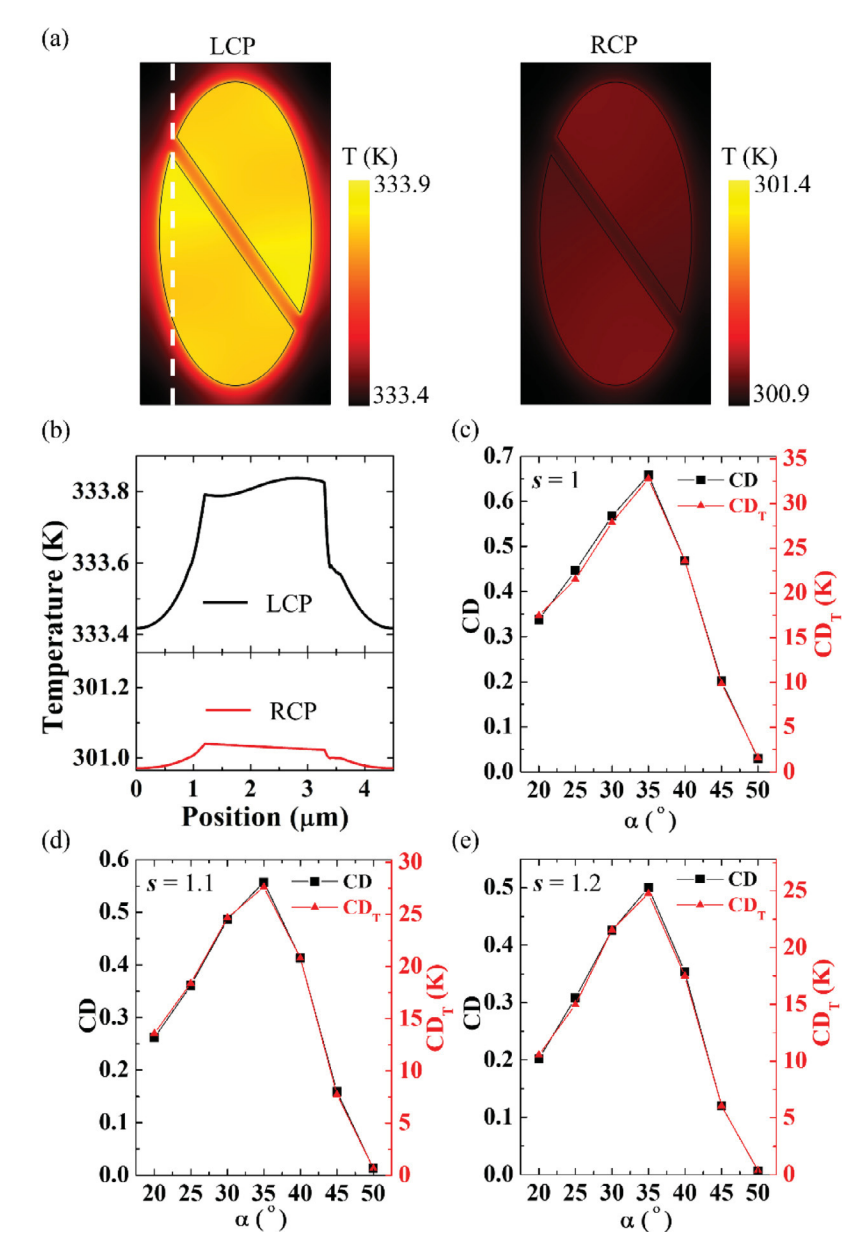


Fig. 8. (a) Temperature distributions at z=450 nm plane with LCP and RCP illumination at the chiral resonance of 5.04 μm. (b) Temperature profiles across the tip of split-ellipse structure at x=400 nm which is marked with the white dashed line in (a). (c)–(e) Simulated values of CD in absorption and CD_T as a function of the rotation angle α for different scale factors s of 1, 1.1 and 1.2, respectively. Black squares and red triangles represent the calculated data points of CD in absorption and CD_T, respectively.

averaged value of 28.28 K $\mu m^2/\mu W$ which is independent of the chiral resonance wavelength and the CD value for all the chiral metasurface absorbers with different geometries.

3. Conclusion

In summary, mid-infrared chiral plasmonic metasurface absorbers have been designed and demonstrated with high CD in absorption across the wavelength range of 5 to 5.9 μ m. The electric field distributions in the chiral metasurface absorber under LCP and RCP illumination have been studied to understand the mechanism of the strong chiral optical absorption. The chiral resonance wavelength and the CD in absorption can be tuned by adjusting the geometric parameters of the split-ellipse structure. Compared to the previously demonstrated chiral metasurface absorbers with other types of asymmetric structures such as the F-shaped structure [6], the coupled rectangle bars [29], and the eye-shaped structure [30], the CD value of the chiral metasurface absorber made of the split-ellipse structure can be continuously tuned

by simply adjusting the rotation angle of the cutting slot without changing other geometric parameters. Furthermore, the heat transfer analysis is conducted to show the temperature distributions in the metasurface absorber under LCP and RCP illumination and reveal the linear relationship between CD in absorption and CD_{T} . These results will advance many future applications including chemical and biological chiral sensing, thermal radiation, chiral imaging and spectroscopy.

Declaration of competing interest

The authors declare that they have no known competing financial interests or personal relationships that could have appeared to influence the work reported in this paper.

Data availability

Data will be made available on request.

Acknowledgments

The authors acknowledge support from the National Science Foundation, USA (Grant No. DMR-1552871 and ECCS-1653032). This work was performed, in part, at the Center for Nanoscale Materials, a U.S. Department of Energy Office of Science User Facility, and supported by the U.S. Department of Energy, Office of Science (Contract No. DE-AC02-06CH11357). The authors also acknowledge the support from the Intelligent Systems Center and the facility support from the Materials Research Center at Missouri S&T.

References

- A.J. Miles, B.A. Wallace, Circular dichroism spectroscopy of membrane proteins, Chem. Soc. Rev. 45 (2016) 4859–4872, http://dx.doi.org/10.1039/C5CS00084J.
- [2] M. Vorlíčková, I. Kejnovská, K. Bednářová, D. Renčiuk, J. Kypr, Circular dichroism spectroscopy of DNA: from duplexes to quadruplexes, Chirality 24 (2012) 691–698, http://dx.doi.org/10.1002/chir.22064.
- [3] I. Tinoco Jr., Application of optical rotatory dispersion and circular dichrosim to the study of biopolymers, Methods Biochem Anal. 18 (1970) 81–203, http: //dx.doi.org/10.1002/9780470110362.ch3.
- [4] C. Helgert, E. Pshenay-Severin, M. Falkner, C. Menzel, C. Rockstuhl, E.B. Kley, A. Tünnermann, F. Lederer, T. Pertsch, Chiral metamaterial composed of threedimensional plasmonic nanostructures, Nano Lett. 11 (2011) 4400–4404, http: //dx.doi.org/10.1021/nl202565e.
- [5] B. Tang, Z. Li, E. Palacios, Z. Liu, S. Butun, K. Aydin, Chiral-selective plasmonic metasurface absorbers operating at visible frequencies, IEEE Photonics Technol. Lett. 29 (2017) 295–298, http://dx.doi.org/10.1109/LPT.2016.2647262.
- [6] M.S. Mahmud, D. Rosenmann, D.A. Czaplewski, J. Gao, X. Yang, Chiral plasmonic metasurface absorbers in the mid-infrared wavelength range, Opt. Lett. 45 (2020) 5372–5375, http://dx.doi.org/10.1364/OL.404192.
- [7] T. Cao, L. Zhang, R.E. Simpson, C. Wei, M.J. Cryan, Strongly tunable circular dichroism in gammadion chiral phase-change metamaterials, Opt. Express 21 (2013) 27841–27851, http://dx.doi.org/10.1364/OE.21.027841.
- [8] S. Yang, Z. Liu, S. Hu, A.-Z. Jin, H. Yang, S. Zhang, J. Li, C. Gu, Spin-selective transmission in chiral folded metasurfaces, Nano Lett. 19 (2019) 3432–3439, http://dx.doi.org/10.1021/acs.nanolett.8b04521.
- [9] L. Wang, X. Huang, M. Li, J. Dong, Chirality selective metamaterial absorber with dual bands, Opt. Express 27 (2019) 25983–25993, http://dx.doi.org/10. 1364/OE.27.025983.
- [10] Y. Chen, X. Yang, J. Gao, 3D Janus plasmonic helical nanoapertures for polarization-encrypted data storage, Light Sci. Appl. 8 (2019) 45, http://dx.doi. org/10.1038/s41377-019-0156-8.
- [11] Y. Chen, J. Gao, X. Yang, Chiral grayscale imaging with plasmonic metasurfaces of stepped nanoapertures, Adv. Opt. Mater. 7 (2019) 1801467, http://dx.doi. org/10.1002/adom.201801467.
- [12] C. Sabah, F. Dincer, M. Karaaslan, M. Bakir, E. Unal, O. Akgol, Biosensor applications of chiral metamaterials for marrowbone temperature sensing, J. Electromagn. Waves Appl. 29 (2015) 2393–2403, http://dx.doi.org/10.1080/09205071.2015.1084894.
- [13] S. Asgari, N. Granpayeh, T. Fabritius, Controllable terahertz cross-shaped three-dimensional graphene intrinsically chiral metastructure and its biosensing application, Opt. Commun. 474 (2020) 126080, http://dx.doi.org/10.1016/j. optcom.2020.126080.

- [14] T. Iida, A. Ishikawa, T. Tanaka, A. Muranaka, M. Uchiyama, Y. Hayashi, K. Tsuruta, Super-chiral vibrational spectroscopy with metasurfaces for highsensitive identification of alanine enantiomers, Appl. Phys. Lett. 117 (2020) 101103, http://dx.doi.org/10.1063/5.0012331.
- [15] J. García-Guirado, M. Svedendahl, J. Puigdollers, R. Quidant, Enantiomer-selective molecular sensing using racemic nanoplasmonic arrays, Nano Lett. 18 (2018) 6279–6285, http://dx.doi.org/10.1021/acs.nanolett.8b02433.
- [16] M. Manoccio, M. Esposito, E. Primiceri, A. Leo, V. Tasco, M. Cuscunà, D. Zuev, Y. Sun, G. Maruccio, A. Romano, A. Quattrini, G. Gigli, A. Passaseo, Femtomolar biodetection by a compact core-shell 3D chiral metamaterial, Nano Lett. 21 (2021) 6179–6187, http://dx.doi.org/10.1021/acs.nanolett.1c01791.
- [17] J. Mun, M. Kim, Y. Yang, T. Badloe, J. Ni, Y. Chen, C.W. Qiu, J. Rho, Electro-magnetic chirality: from fundamentals to nontraditional chiroptical phenomena, Light Sci. Appl. 9 (2020) 1–18.
- [18] J. Zhou, T. Koschny, M. Kafesaki, E.N. Economou, J.B. Pendry, C.M. Soukoulis, Saturation of the magnetic response of split-ring resonators at optical frequencies, Phys. Rev. Lett. 95 (2005) 223902, http://dx.doi.org/10.1103/PhysRevLett.95. 223902
- [19] X.T. Kong, L. Khosravi Khorashad, Z. Wang, A.O. Govorov, Photothermal circular dichroism induced by plasmon resonances in chiral metamaterial absorbers and bolometers, Nano Lett. 18 (2018) 2001–2008, http://dx.doi.org/10.1021/acs. nanolett.7b05446.
- [20] T. Lv, Y. Li, H. Ma, Z. Zhu, Z. Li, C. Guan, J. Shi, H. Zhang, T. Cui, Hybrid metamaterial switching for manipulating chirality based on VO2 phase transition, Sci. Rep. 6 (2016) 1–9, http://dx.doi.org/10.1038/srep23186.
- [21] Y. Ren, T. Zhou, C. Jiang, B. Tang, Thermally switching between perfect absorber and asymmetric transmission in vanadium dioxide-assisted metamaterials, Opt. Express 29 (2021) 7666–7679, http://dx.doi.org/10.1364/OE.418273.
- [22] S. Guddala, R. Kumar, S.A. Ramakrishna, Thermally induced nonlinear optical absorption in metamaterial perfect absorbers, Appl. Phys. Lett. 106 (2015) 111901, http://dx.doi.org/10.1063/1.4914451.
- [23] L. Ouyang, W. Wang, D. Rosenmann, D.A. Czaplewski, J. Gao, X. Yang, Near-infrared chiral plasmonic metasurface absorbers, Opt. Express 26 (2018) 31484–31489, http://dx.doi.org/10.1364/OE.26.031484.
- [24] S. Yoo, Q.H. Park, Metamaterials and chiral sensing: a review of fundamentals and applications, Nanophotonics 8 (2019) 249–261.
- [25] Y.Y. Lee, R.M. Kim, S.W. Im, M. Balamurugan, K.T. Nam, Plasmonic metamaterials for chiral sensing applications, Nanoscale 12 (2020) 58–66, http: //dx.doi.org/10.1039/C9NR08433A.
- [26] J. Kischkat, S. Peters, B. Gruska, M. Semtsiv, M. Chashnikova, M. Klinkmüller, O. Fedosenko, S. Machulik, A. Aleksandrova, G. Monastyrskyi, Mid-infrared optical properties of thin films of aluminum oxide titanium dioxide, silicon dioxide, aluminum nitride, and silicon nitride, Appl. Opt. 51 (2012) 6789–6798, http://dx.doi.org/10.1364/AO.51.006789.
- [27] A.D. Rakić, A.B. Djurišić, J.M. Elazar, M.L. Majewski, Optical properties of metallic films for vertical-cavity optoelectronic devices, Appl. Opt. 37 (1998) 5271–5283, http://dx.doi.org/10.1364/AO.37.005271.
- [28] L. Ouyang, D. Rosenmann, D.A. Czaplewski, J. Gao, X. Yang, Broadband infrared circular dichroism in chiral metasurface absorbers, Nanotechnology 31 (2020) 295203
- [29] H. Tang, D. Rosenmann, D.A. Czaplewski, X. Yang, J. Gao, Dual-band selective circular dichroism in mid-infrared chiral metasurfaces, Opt. Express 30 (2022) 20063–20075, http://dx.doi.org/10.1364/OE.457218.
- [30] S. Mahmud, D. Rosenmann, D.A. Czaplewski, J. Gao, X. Yang, Plasmon-phonon coupling between mid-infrared chiral metasurfaces and molecular vibrations, Opt. Express 28 (2020) 21192–21201, http://dx.doi.org/10.1364/OE.397725.